Supplementary material for Impact of topography on earthquake static slip estimates

Contents

S1. Data and forward model for the 2015 Gorkha event

The Gorkha event has been well recorded by various types of geodetic data, such as static GPS offsets and synthetic aperture radar (InSAR).

In this study, we use the static GPS offsets processed and provided by Galetzka et al. (2015) and Yadav et al. (2017).

We also use three InSAR frames that are detailed in Table S1. The ALOS-2 data were collected by the Japan Aerospace Exploration Agency (JAXA) and processed by Lindsey et al. (2015). The Sentinel-1 data were collected by the European Space Agency and processed by Grandin et al. (2015). To improve computational efficiency, we resample InSAR observations based on model resolution (Lohman and Simons, 2005) with windows ranging from 30 km to 2 km. We account for measurement uncertainties by building a data covariance matrix. To do so, we mask the area of coseismic displacement and estimate empirical covariograms as a function of distance between data points (Figure S1). Then, the InSAR covariance matrix $\mathbf{C}_{\mathrm{d}}^{\mathrm{insar}}$ is calculated from the best fitting exponential function to empirical covariograms (Jolivet et al., 2012).

We also account for the uncertainty due to our a priori assumed fault geometry (Ragon et al., 2018, 2019). We assume conservative uncertainty values of (-1°, 1°) around the prior value for the

fault dip and (-1 km, 1 km) for the fault position. The sensitivity of the Green's functions (GFs) to a variation in fault geometry is estimated from non-topographic GFs for every case. We adopt this approximation for simplicity, and because we assume that small perturbations of the GFs due to a change in fault geometry are close whether topography is introduced or not. The conservative uncertainty values assumed and the good data coverage of this event makes the impact of these uncertainties on inferred slip models very limited.

Satellite (orbit pass)	Track	Interferogram pair
ALOS 2 (ascending)	T157	02/21/2015 - 05/02/2015
ALOS 2 (descending)	T048	04/05/2015 - 05/03/2015
Sentinel 1A (ascending)	TN117	04/09/2015 - 05/03/2015

Table 1: Interferometric pairs used for the 2015 Gorkha event

Specifications	Values
Domain coordinates	83.5°E 87.5°E 26.6°N 29.2°N
Domain size	$390 \times 280 \times 83$ km
Mesh spacing	3 km
Number of elements	323830
Poisson's ratio	0.25
Young's modulus	82.4 GPa

Table 2: Model domain, mesh and material properties assumed for the Gorkha event

Parameter	Values
Length	180 km
Width	100 km
Number of subfaults along strike	18
Number of subfaults along dip	10
Strike	285°
Dip	7°
Northernmost point longitude	86.118721°E
Northernmost point latitude	27.280154°N
Depth of fault tip	3.656 km

Table 3: Fault geometry parameters assumed for the Gorkha event

S2. Figures S1 to S3: Data and forward model for the 2015 Gorkha earthquake

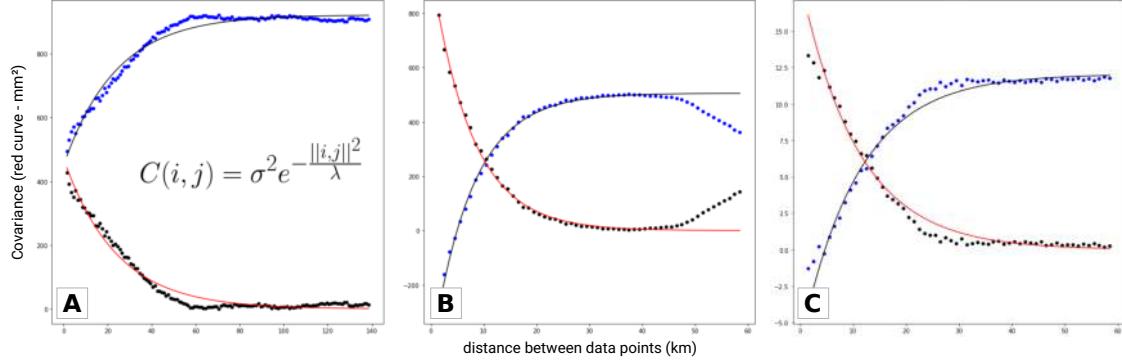$$C(i,j) = \sigma^2 e^{-\frac{||i,j||^2}{\lambda}}$$

Figure S1: Empirical covariance functions for the interferograms used in the study of the Gorkha earthquake. Radially symmetric empirical covariance functions (black points) and associated best fit exponential functions (red curve) for the displacements derived from InSAR data. For each interferogram, we compute the empirical covariance as a function of the inter-pixel distance and then fit an exponential function (Jolivet et al. 2012). The exponential function is used to build the data covariance matrix. (A) for the ALOS2 T048 interferogram, with the exponential function characterized by $\lambda = 0.2$ km and $\sigma = 427.4$ mm. (B) for the ALOS2 T157 interferogram, with $\lambda = 7.65$ km and $\sigma = 31.05$ mm. (C) for the Sentinel 1 interferogram, with $\lambda = 10.94$ km and $\sigma = 4.29$ mm.
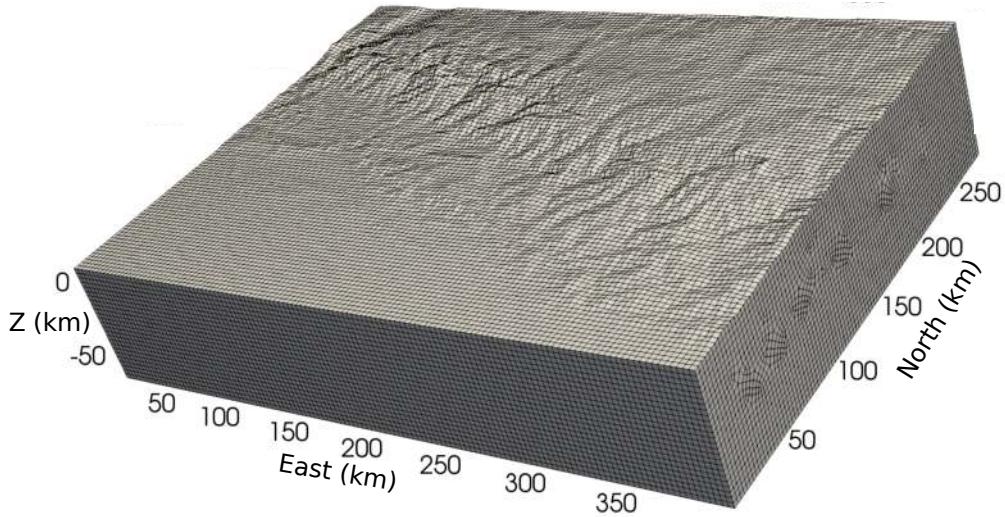

Figure S2: Topographic mesh used to calculate Green's functions with topography for the Gorkha event. This mesh was produced using Trelis 13.0
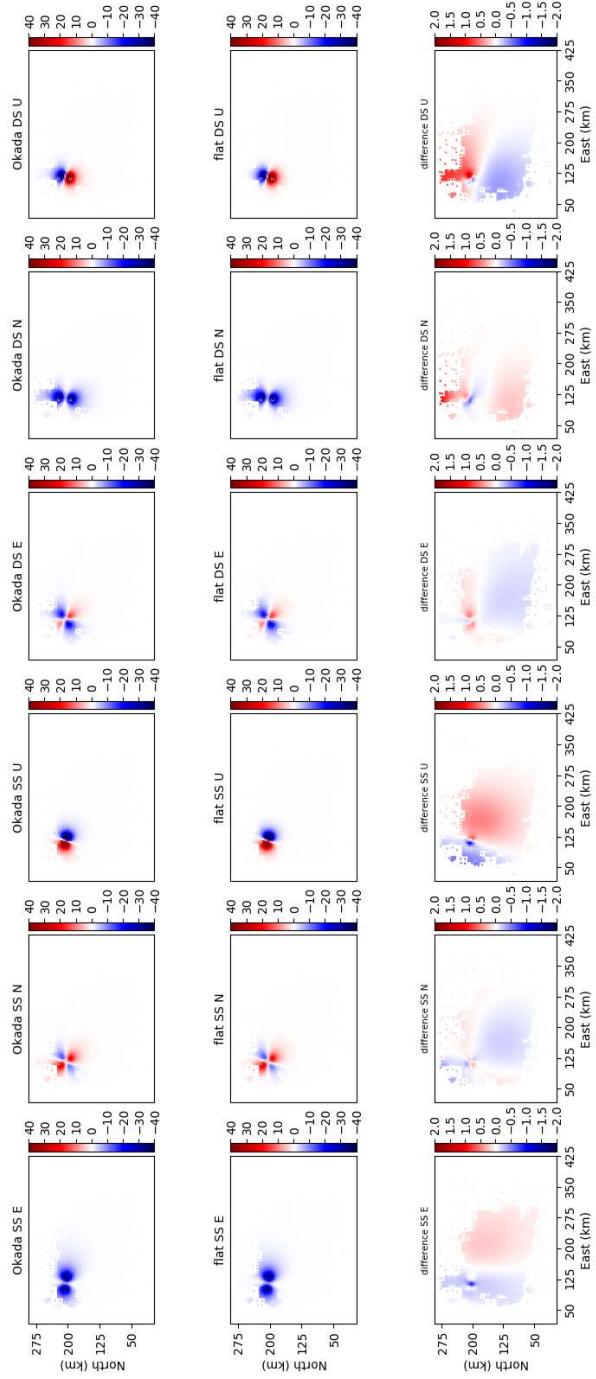
Figure S3: Benchmark for Gorkha Green's functions. The top row shows Green's functions calculated with Okada and the middle row shows Green's functions calculated using SPECFEM-X with a non-topographic mesh. The bottom row shows the difference, with color scale magnified by 20×. Units of color bars are in millimeters. These differences are very small – not more than a few percent – so we can safely compare Okada Green's functions to SPECFEM-X 3D Green's functions.

S3. Text S2: Data and forward model for the 2010 Maule event

Our data consists of 53 static daily offsets processed by Vigny et al. (2011), and continuous GPS and survey sites processed by Lin et al. (2013). We derive observational errors from processing errors, but also consider additional uncertainty (0.5 cm for vertical displacement and 2 cm for horizontal displacement) based on the assumption that GPS might not only measure tectonic but also local deformation signals.

We also account for the uncertainty due to our a priori assumed fault geometry (Ragon et al., 2018, 2019). We assume conservative uncertainty values of (-1°, 1°) around the prior value for the fault dip and (0 km, 2 km) for the fault position. Note that these uncertainties are not sufficient to cancel out the fact that our assumed structure is an over-simplified approximation of reality. However, these additional uncertainties help broaden the exploration of the solution space.

Specifications	Values
Domain coordinates	-75.0°E -68.5°E -40.3°N -31.5°N
Domain size	$553 \times 958 \times 136$ km
Mesh spacing	6 km
Number of elements	318400
Poisson's ratio	0.25
Young's modulus	100.0 GPa

Table 4: Model domain, mesh and material properties used for the Maule event

Parameter	Values	
Length	570 km	
Width	240 km	
Strike	198°	
Dip	18°	
Northernmost point longitude	-74.78718°E	
Northernmost point latitude	-37.70672°N	
Depth of fault tip	9.760 km	
	Near-trench row	**Deeper rows**
Number of subfaults along strike	7	13
Number of subfaults along dip	1	8
Subfault size (along dip - along strike)	81.4 x 48 km	43.8 x 24 km

Table 5: Fault geometry parameters used for the Maule event

S4. Figures S4 to S12: Fit to the observations or synthetic dataset for the 2015 Gorkha earthquake
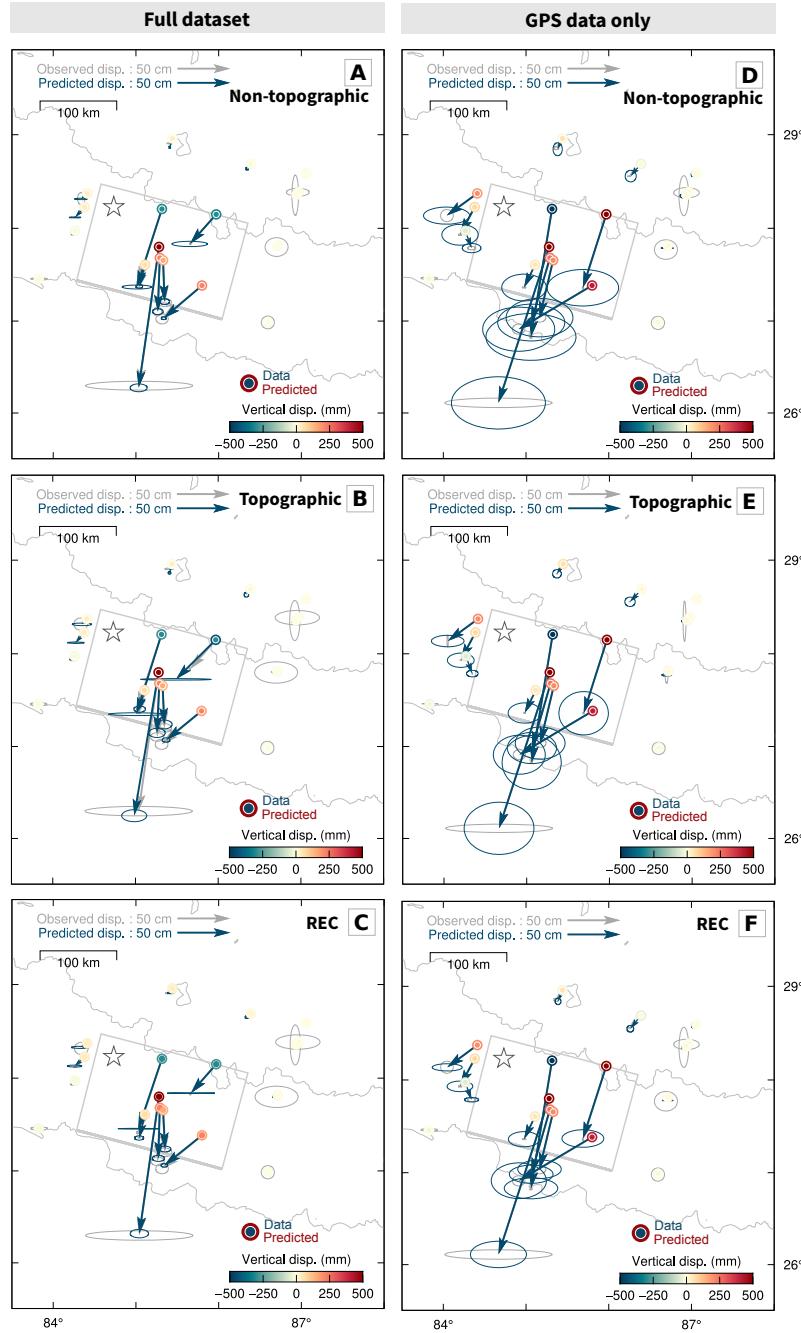
Figure S4: Synthetic (derived from the target slip models presented in Figure 3) and predicted GPS offsets for the 2015 Gorkha event, using either non-topographic (A, D), topographic (B, E) or REC Green's functions (C, F), and for inversions using either the full synthetic dataset (GPS and InSAR, left) or the synthetic GPS dataset only (right). Predictions are inferred from the average model. Observed horizontal surface displacements are in gray with 95% confidence ellipses, and predicted displacements are in blue with 95% confidence ellipses. Vertical displacements are color-coded with color scale truncated at (-1 m, 1 m). The inner circle represents the data and the outer circle represents predicted displacements. The assumed fault geometry is shown as a gray rectangle, and the epicenter is the white star.
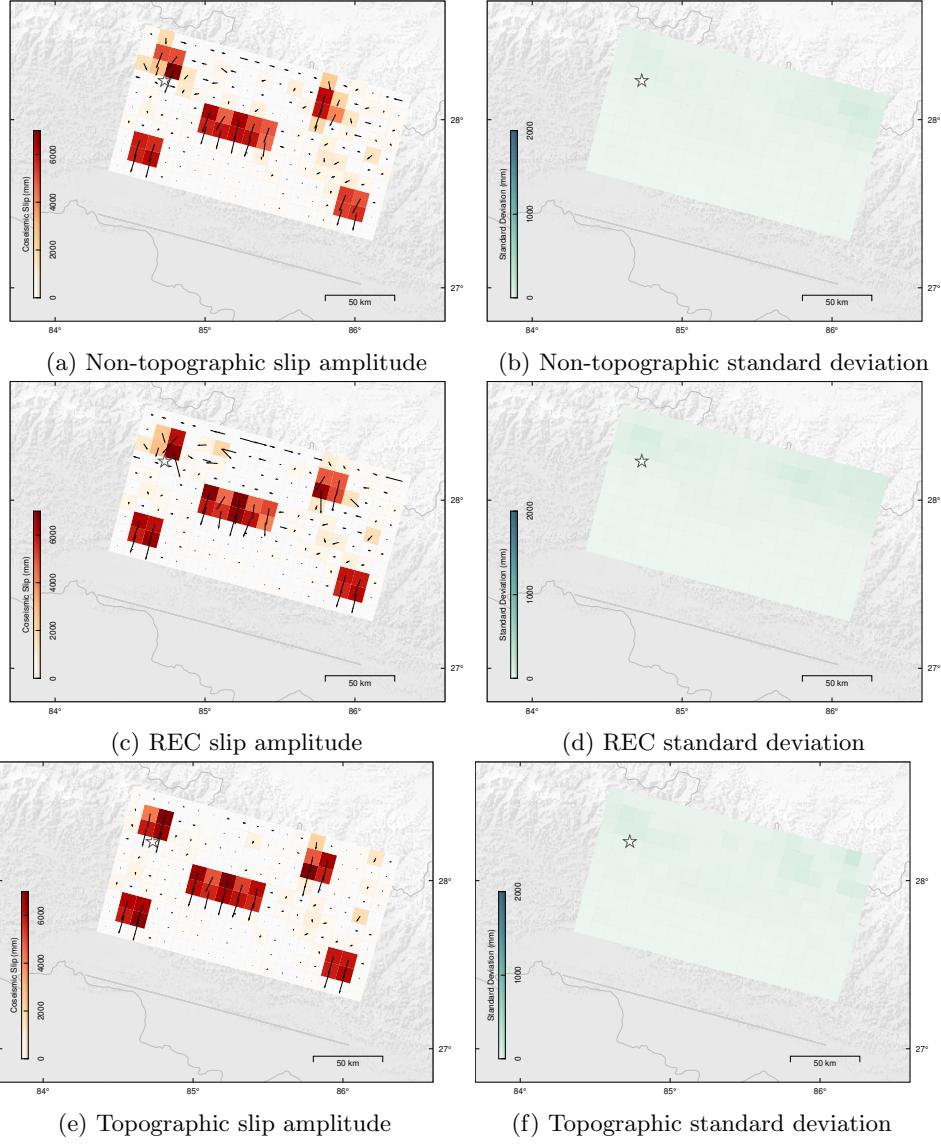
(a) Non-topographic slip amplitude

(b) Non-topographic standard deviation

(c) REC slip amplitude

(d) REC standard deviation

(e) Topographic slip amplitude

(f) Topographic standard deviation

Figure S5: Slip models estimated from the full noisy synthetic dataset for the target model shown in Fig 3.
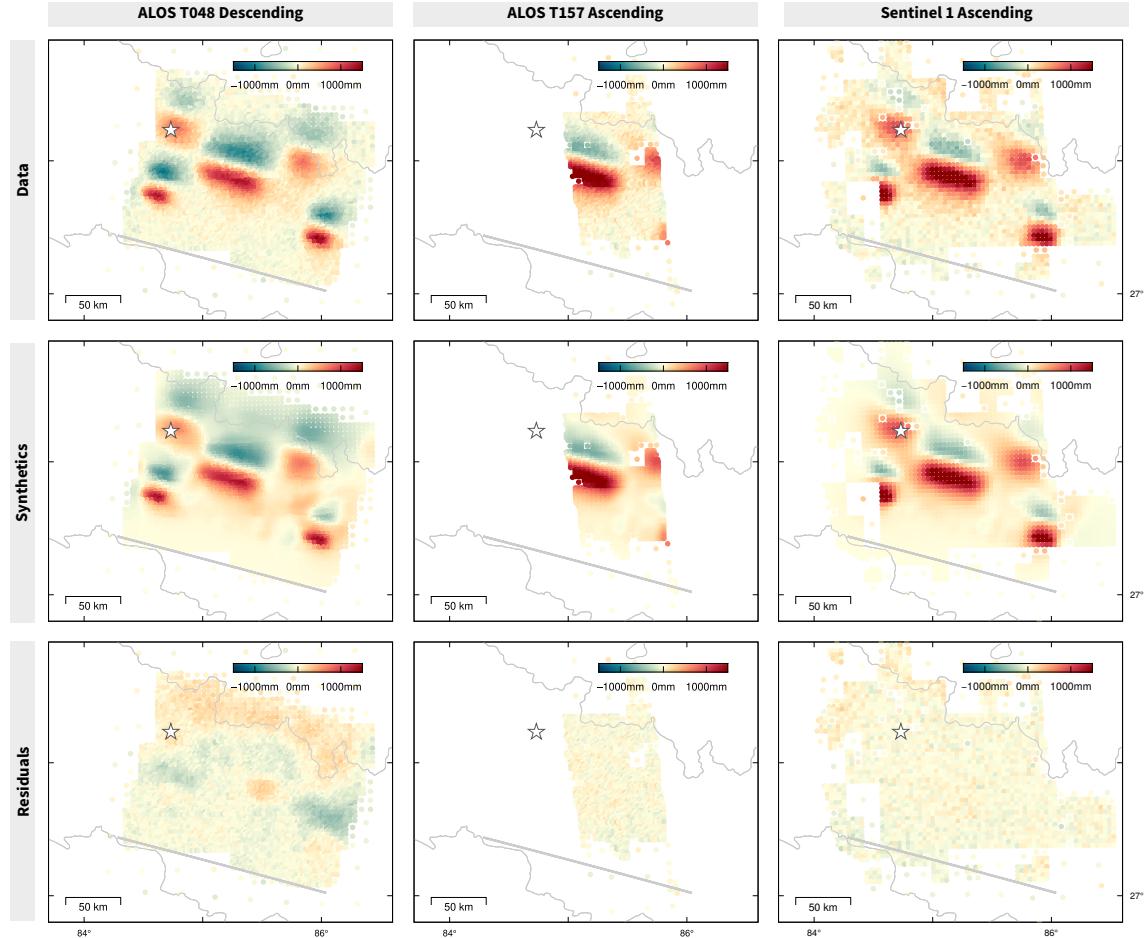
8

Figure S6: Fit to the synthetic noisy InSAR dataset for the inferred model presented in Fig S5(a), using **non-topographic Green's functions**. Observed surface displacements in the LOS are shown in the top row, predicted displacements are in the middle row, and the residuals are shown in the bottom row. Predictions are inferred from the average model. The assumed fault trace is shown as a dark gray line.
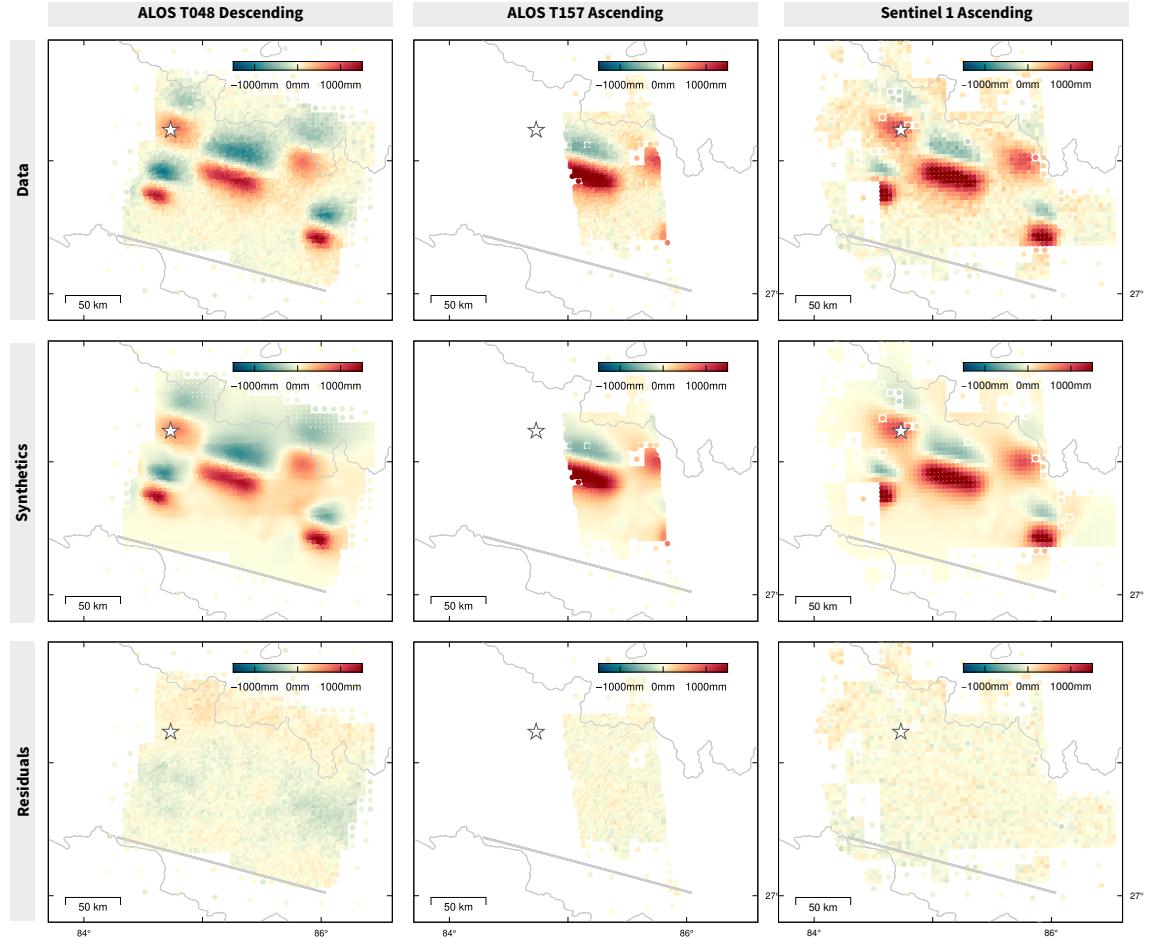
9

Figure S7: Fit to the synthetic noisy InSAR dataset for the inferred model presented in Fig S5(e), using **topographic Green's functions**. Observed surface displacements in the LOS are shown in the top row, predicted displacements are in the middle row, and the residuals are shown in the lower row. Predictions are inferred from the average model. The assumed fault trace is shown as a dark gray line.
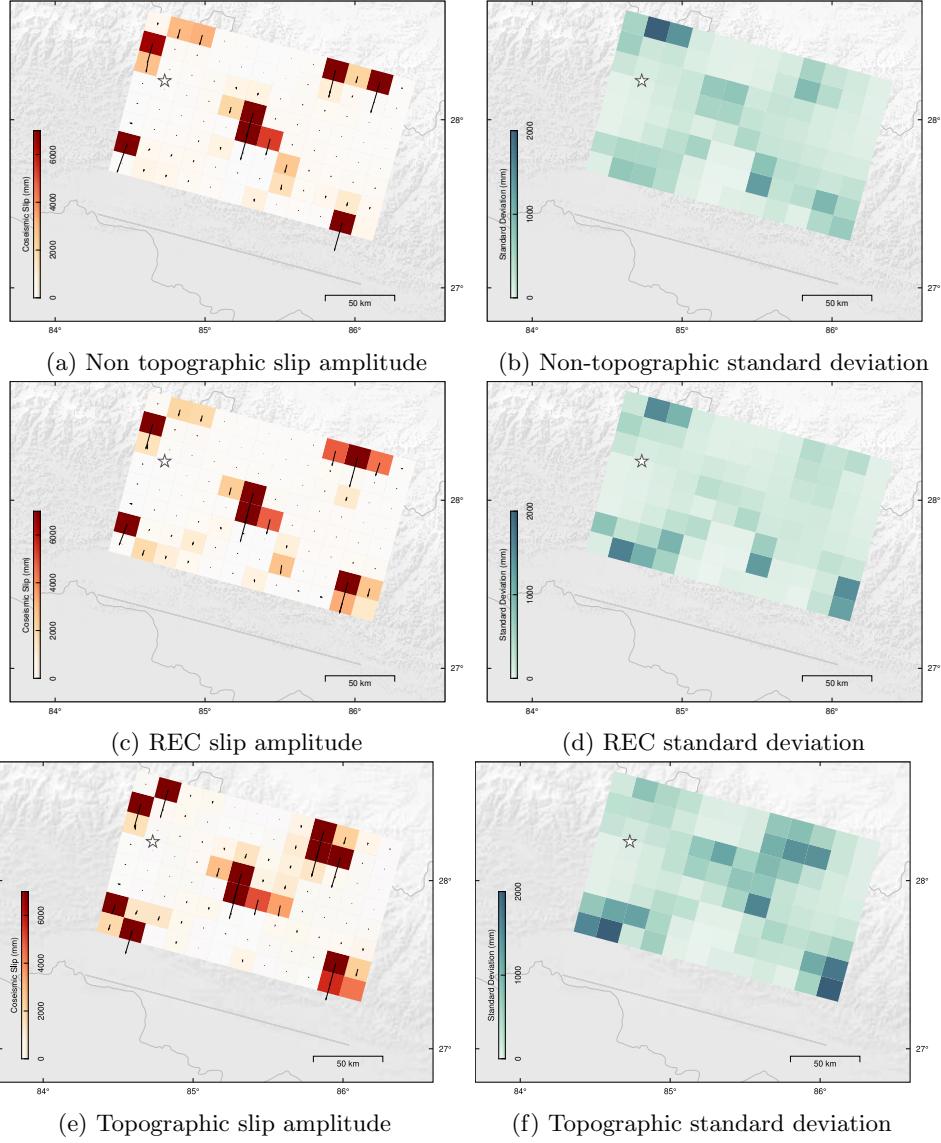
(a) Non topographic slip amplitude

(b) Non-topographic standard deviation

(c) REC slip amplitude

(d) REC standard deviation

(e) Topographic slip amplitude

(f) Topographic standard deviation

Figure S8: Slip models estimated from the GPS-only noisy synthetic dataset for the target model shown in Fig 3.
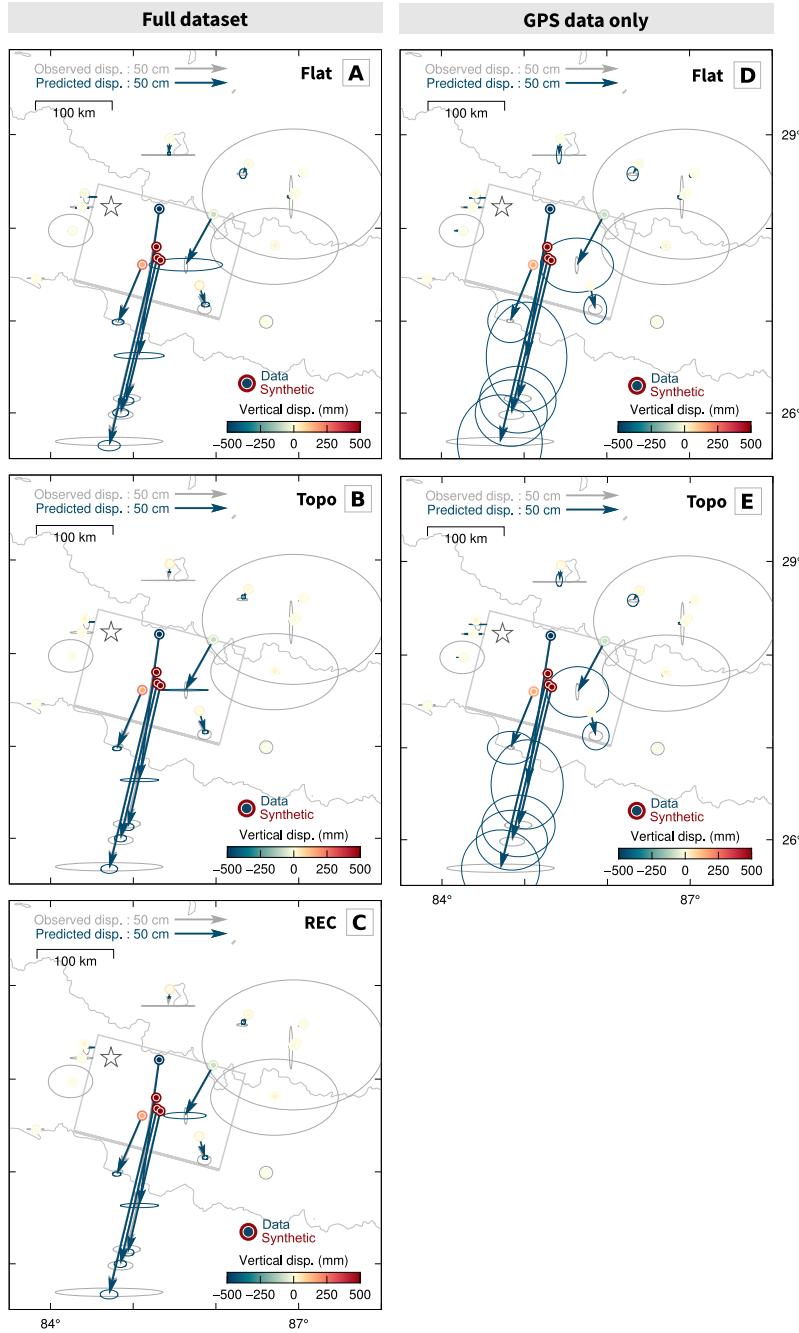
11

Figure S9: Observed and predicted GPS offsets for the 2015 Gorkha event, using either non-topographic (A, D), topographic (B,E) or REC Green's functions (C), and for inversions using either the full dataset (GPS and InSAR, left) or the GPS dataset only (right). Predictions are inferred from the average model. Observed horizontal surface displacements are in gray with 95% confidence ellipses, and predicted displacements are in blue with 95% confidence ellipses. Vertical displacements are color-coded with color-scale truncated at (-1 m, 1 m), the inner round shape representing the data and the outer circle representing the predicted displacements. The assumed fault geometry is shown as a gray rectangle, and the epicenter is the white star.
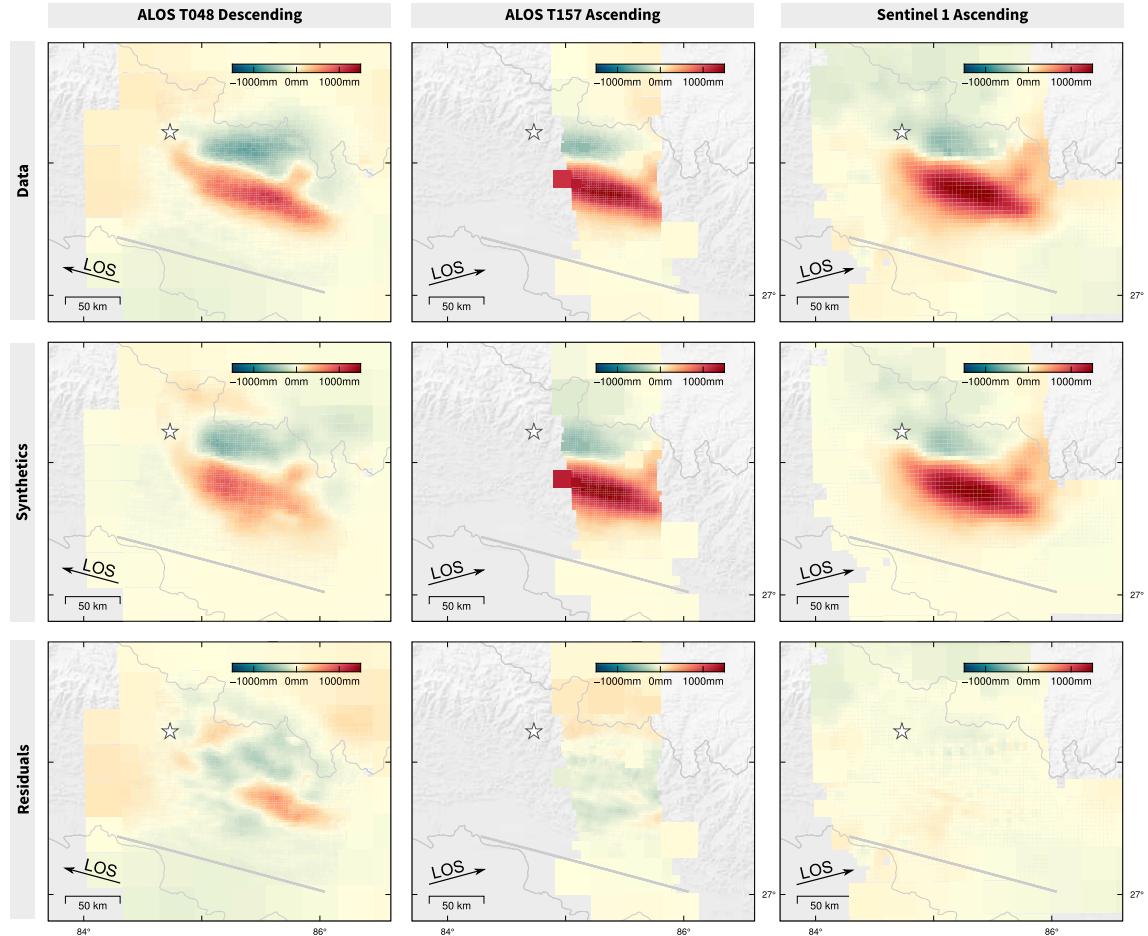
Figure S10: Fit to the InSAR dataset for the 2015 Gorkha event, using **non-topographic Green's functions**. Observed surface displacements in the LOS are shown in the top row, predicted displacements are in the middle row, and the residuals are shown in the bottom row. Predictions are inferred from the average model. The assumed fault trace is shown as a dark gray line.
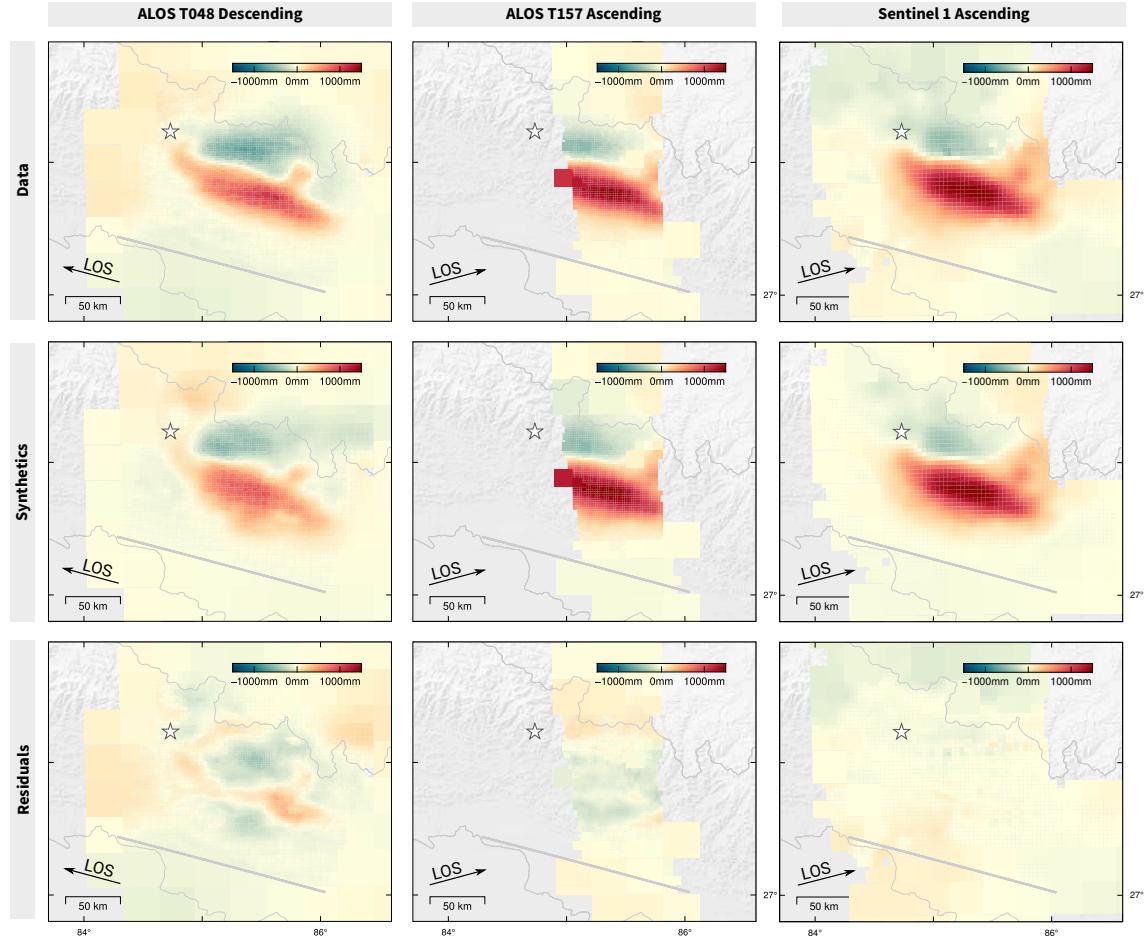
Figure S11: Fit of the InSAR dataset for the 2015 Gorkha event, using **topographic Green's functions**. Observed surface displacements in the LOS are shown in the top row, predicted displacements are in the middle row, and the residuals are shown in the bottom row. Predictions are inferred from the average model. The assumed fault trace is shown as a dark gray line.
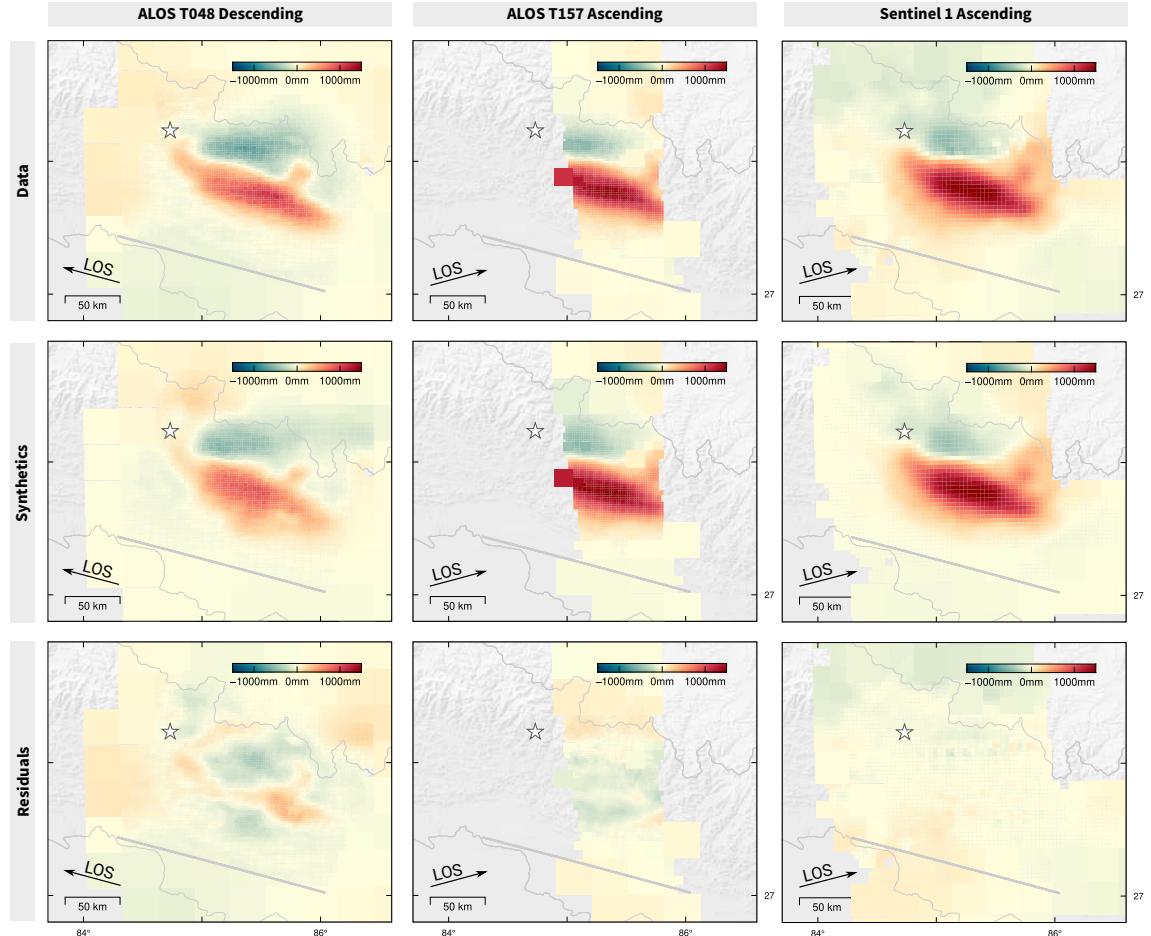
Figure S12: Fit of the InSAR dataset for the 2015 Gorkha event, using **REC Green's functions**. Observed surface displacements in the LOS are shown in the top row, predicted displacements are in the middle row, and the residuals are shown in the bottom row. Predictions are inferred from the average model. The assumed fault trace is shown as a dark gray line.

S5. Figures S16 to S20: Other slip models and fit to the observations or synthetic dataset for the 2010 Maule earthquake
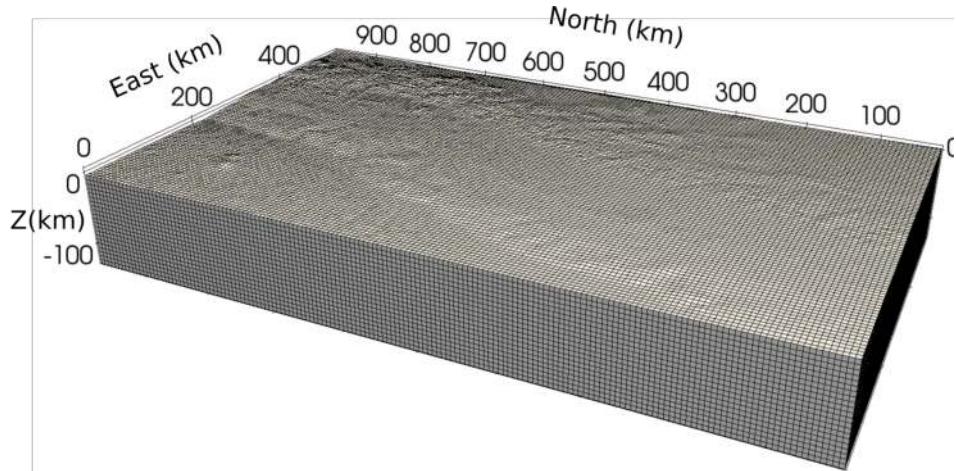

Figure S13: Topographic mesh used to calculate Green's functions with topography for the Maule event. This mesh was produced using Trelis 13.0

(a) Non-topographic slip amplitude

(b) REC slip amplitude

(c) Topographic slip amplitude

(d) Non-topographic standard deviation

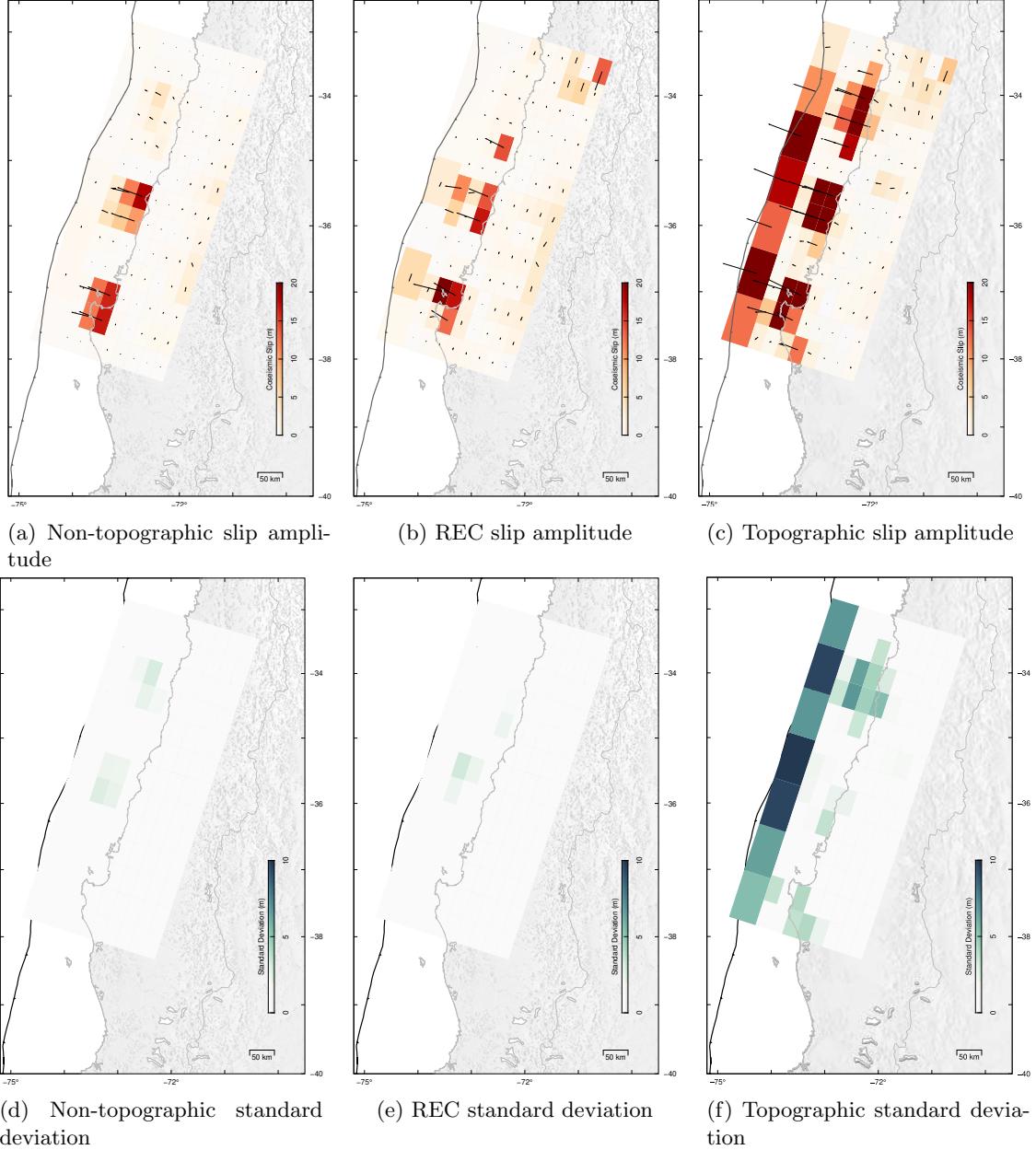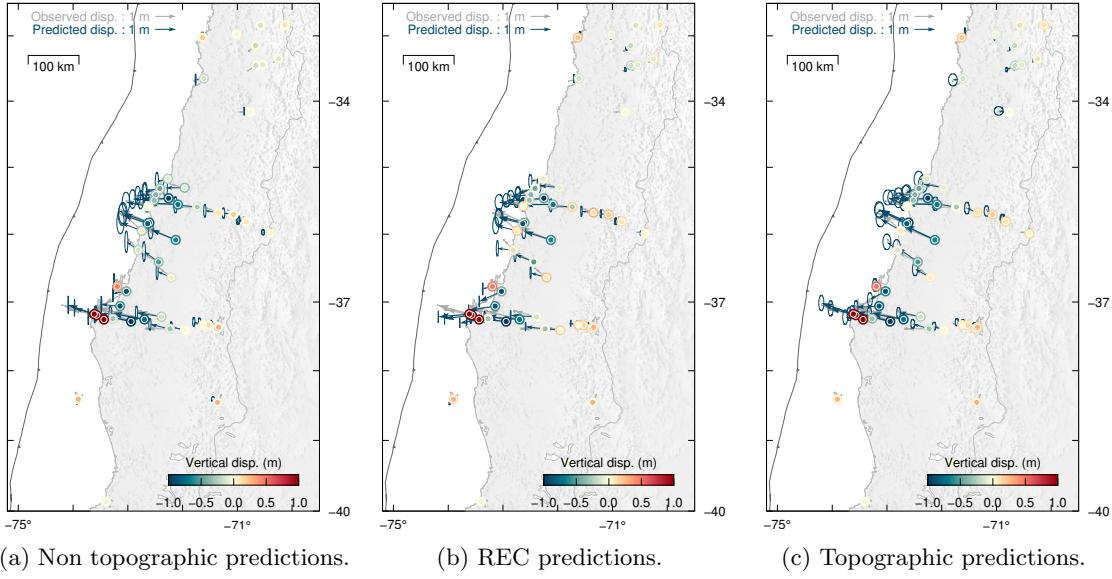(e) REC standard deviation

(f) Topographic standard deviation

Figure S14: Average slip amplitude (total slip) and standard deviation of dip-slip parameters estimated from noisy synthetic data for the Maule earthquake for the target model shown in Figure 7.

(a) Non topographic predictions. (b) REC predictions. (c) Topographic predictions.

Figure S15: Noisy synthetic data (derived from the target slip model presented in Figure 7) and predicted GPS offsets for the 2010 Maule event. Predictions are inferred from the average model. Observed horizontal surface displacements are in gray with 95% confidence ellipses, and predicted displacements are in blue with 95% confidence ellipses. Vertical displacements are color-coded with color scale truncated at (-1 m, 1 m). The inner circle represents the data and the outer circle represents predicted displacements.
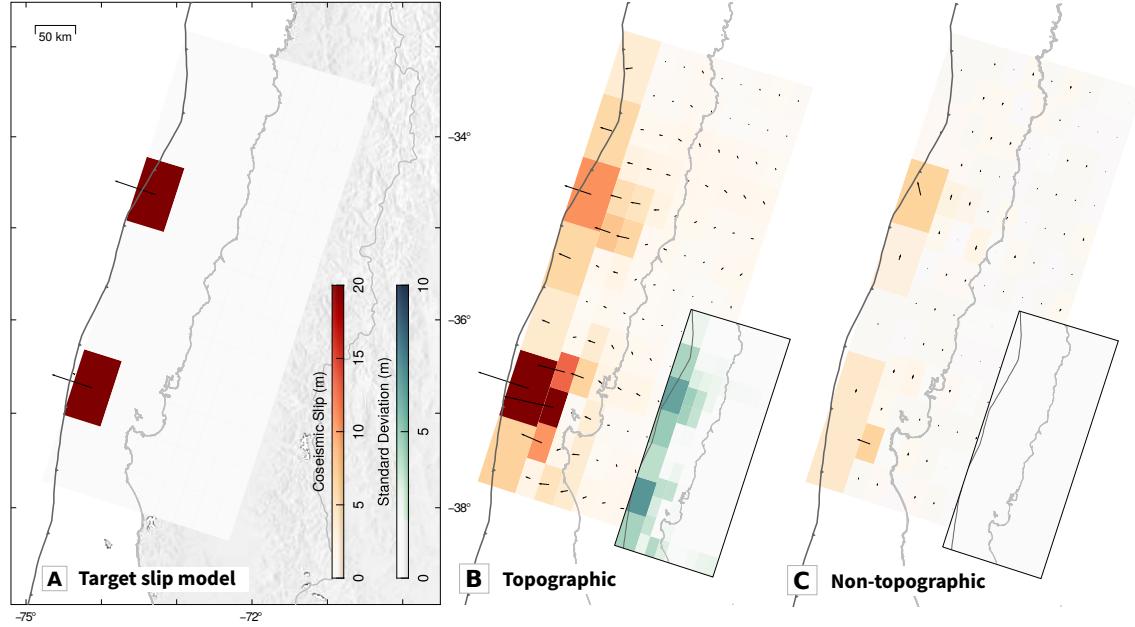

Figure S16: Slip model estimated from synthetic noise-free data for the Maule earthquake for a target model with only near-trench slip patches. (A) Target slip model used to calculate the synthetic data. (B) average slip amplitude (red color scale) and rake estimated with topographic Green's functions. (C) average slip amplitude for non-topographic Green's functions. Posterior standard deviation is shown in green at the bottom right of each slip model.
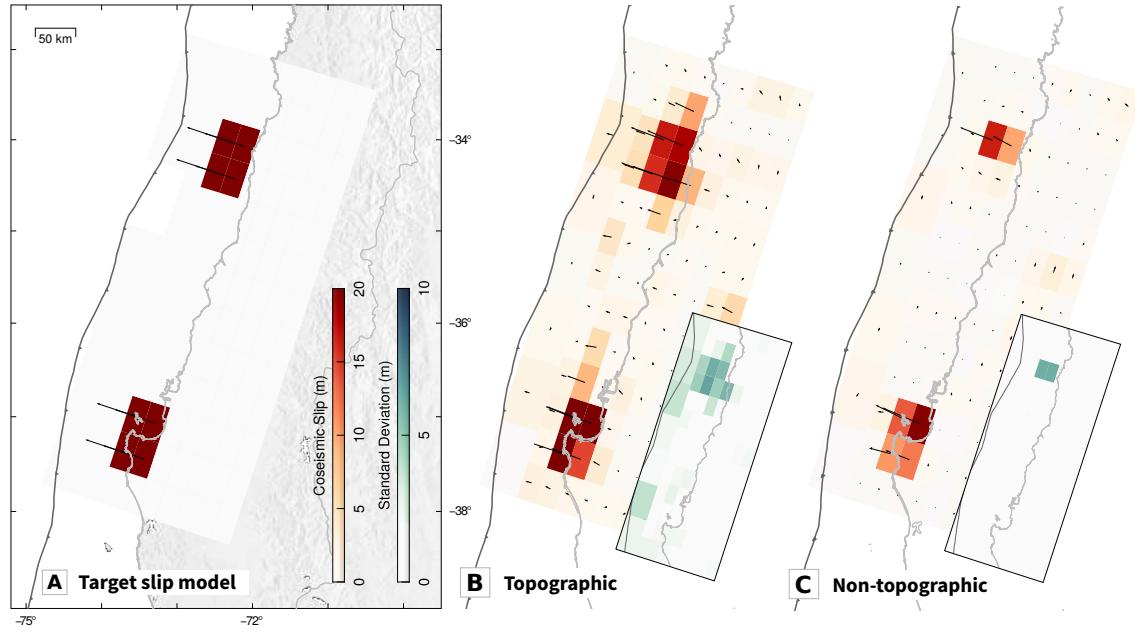
18

Figure S17: Slip model estimated from synthetic noisy data for the Maule earthquake for a target model with only near-coast slip patches. (A) Target slip model used to calculate the synthetic data. (B) average slip amplitude (red color scale) and rake estimated with topographic Green's functions. (C) average slip amplitude for non-topographic Green's functions. Posterior standard deviation is shown in green at the bottom right of each slip model.
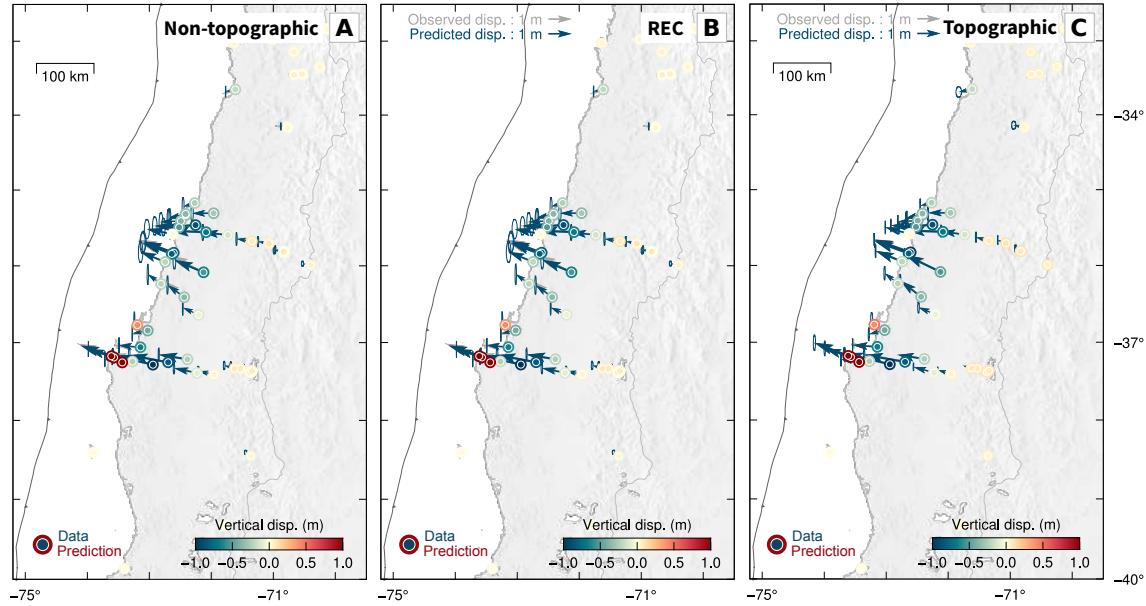

Figure S18: Synthetic (derived from the target slip model presented in Figure 7) and predicted GPS offsets for the 2010 Maule event, using either non-topographic (A), topographic (B) or REC Green's functions (C). Predictions are inferred from the average model. Observed horizontal surface displacements are in gray with 95% confidence ellipses, and predicted displacements are in blue with 95% confidence ellipses. Vertical displacements are color-coded with color-scale truncated at (-1 m, 1 m). The inner circle represents the data and the outer circle represents predicted displacements.
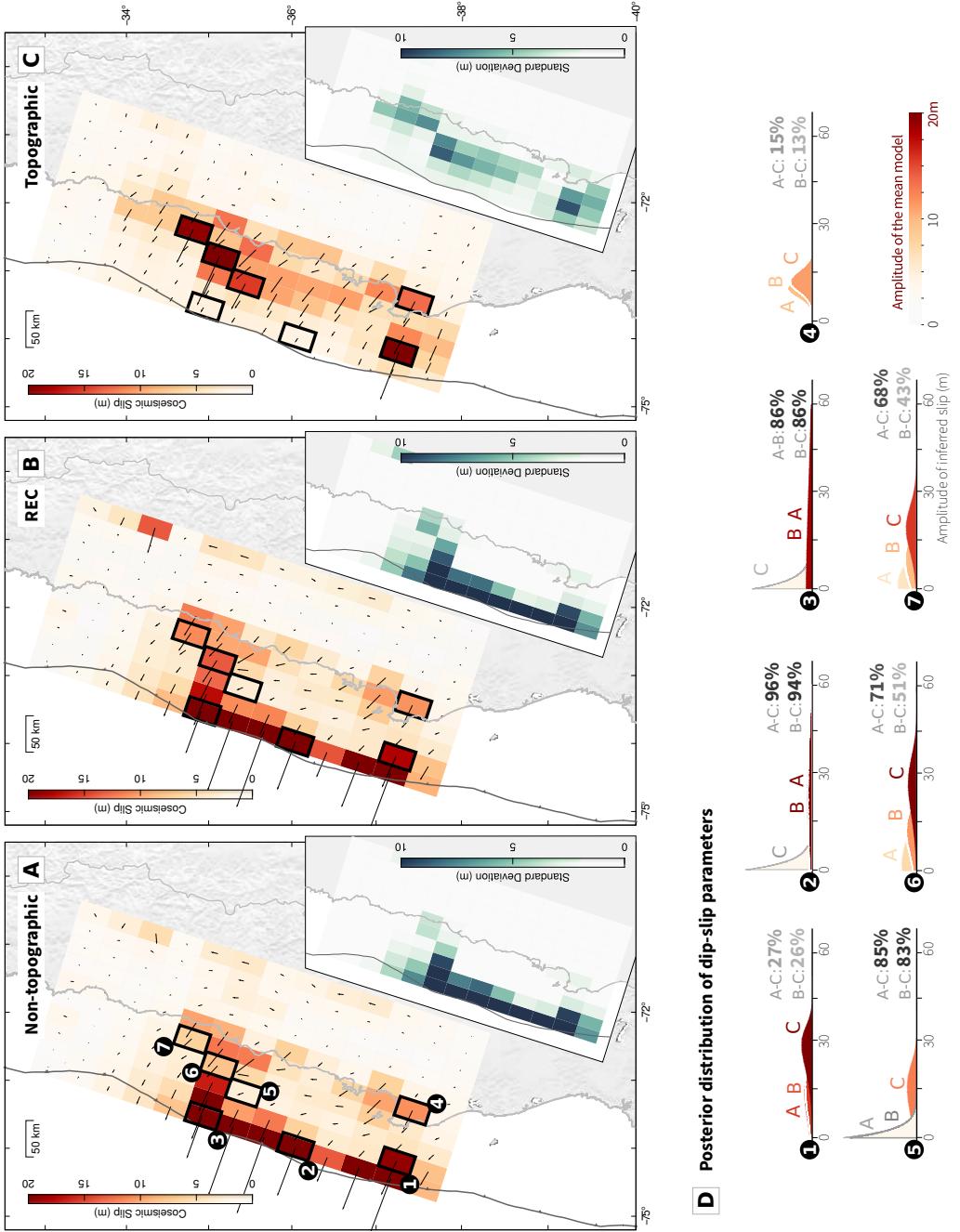
19

Figure S19: (A-C): Average slip models for the 2010 Maule event, assuming smaller subfaults at the trench, and either non-topographic (A), topographic (C) or corrected (B) GFs. The amplitude of slip along dip and the direction of the slip vector are shown in map view. A subfigure also shows the standard deviation of each dip-slip model parameter in green. In (D), the posterior distributions of some chosen dip-slip parameters are shown.
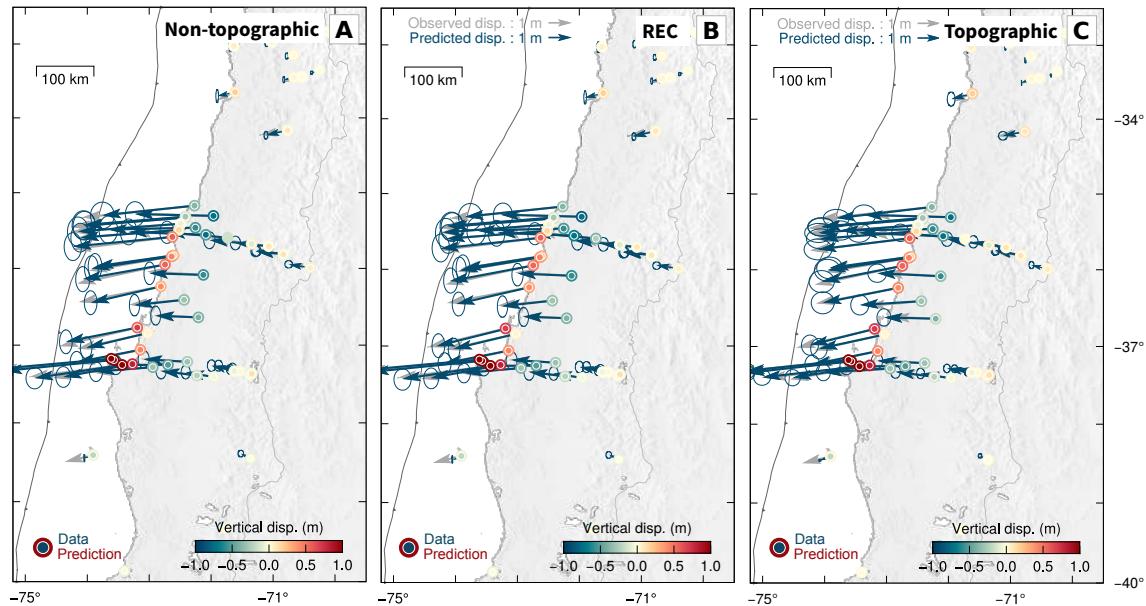
Figure S20: Observed and predicted GPS offsets for the 2010 Maule event, using either non-topographic (A), topographic (B) or REC Green's functions (C). Predictions are inferred from the average model. Observed horizontal surface displacements are in gray with 95% confidence ellipses, and predicted displacements are in blue with 95% confidence ellipses. Vertical displacements are color-coded with color scale truncated at (-1 m, 1 m). The inner circle represents the data and the outer circle represents predicted displacements.

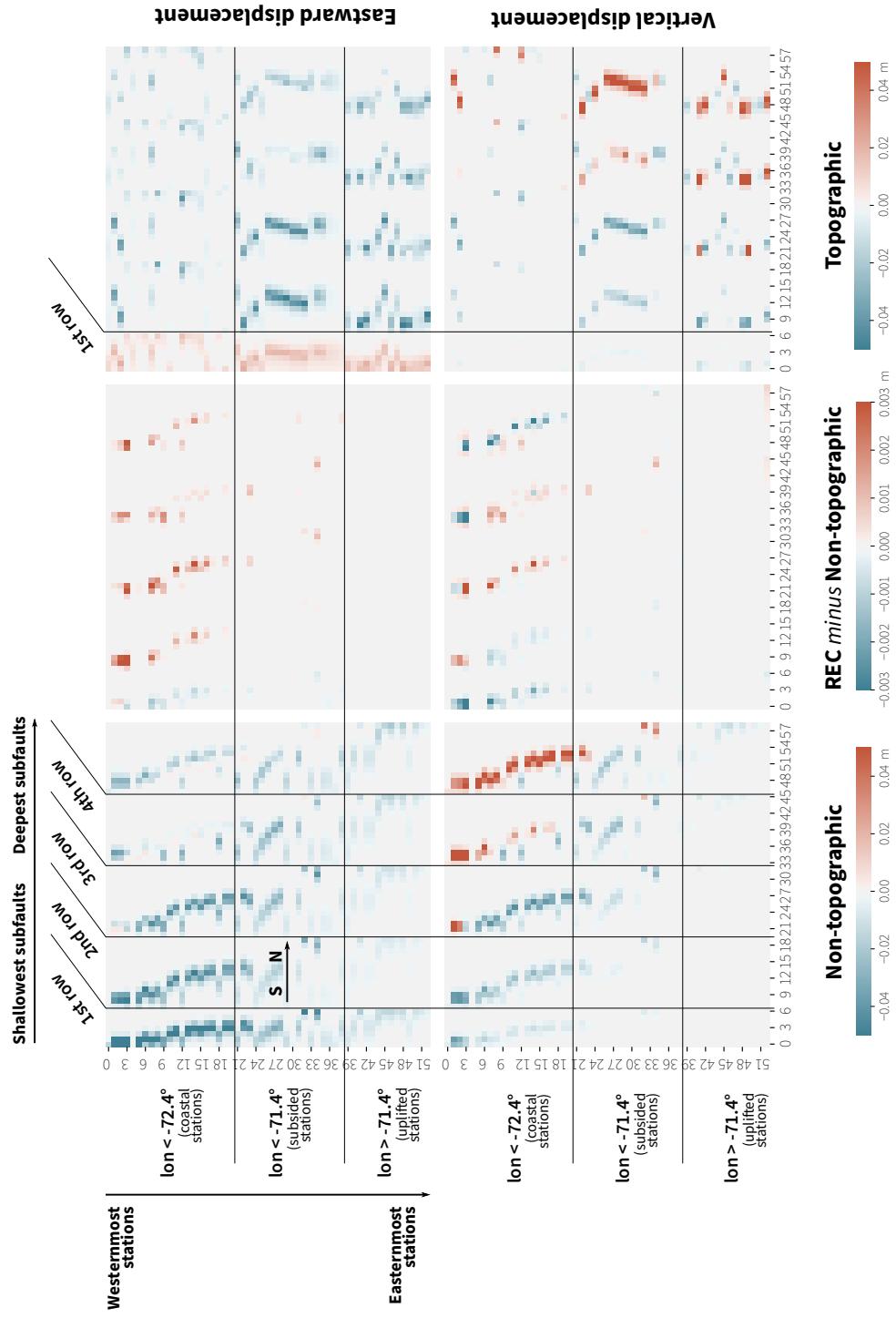Figure S21: Green's functions for the Maule event, computed without topography (left), corrected for topography with the REC method (middle - difference between non-topographic and REC Green's functions), or with topography (right). The Green's functions are shown for the dip-slip parameter of the 4 shallowest subfaults, and the east (top row) or vertical (bottom row) component of the full GPS dataset.

References

Galetzka, J., Melgar, D., Genrich, J.F., Geng, J., Owen, S., Lindsey, E.O., Xu, X., Bock, Y., Avouac, J.P., Adhikari, L.B., Upreti, B.N., Pratt-Sitaula, B., Bhattarai, T.N., Sitaula, B.P., Moore, A., Hudnut, K.W., Szeliga, W., Normandeau, J., Fend, M., Flouzat, M., Bollinger, L., Shrestha, P., Koirala, B., Gautam, U., Bhatterai, M., Gupta, R., Kandel, T., Timsina, C., Sapkota, S.N., Rajaure, S., Maharjan, N., 2015. Slip pulse and resonance of the Kathmandu basin during the 2015 Gorkha earthquake, Nepal. Science 349, 1091–1095. URL: `https://science.sciencemag.org/content/349/6252/1091`, doi:`10.1126/science.aac6383`.

Grandin, R., Valle, M., Satriano, C., Lacassin, R., Klinger, Y., Simoes, M., Bollinger, L., 2015. Rupture process of the Mw=7.9 2015 Gorkha earthquake (Nepal): Insights into Himalayan megathrust segmentation. Geophysical Research Letters 42, 8373–8382. doi:`10.1002/2015gl066044`.

Jolivet, R., Lasserre, C., Doin, M.P., Guillaso, S., Peltzer, G., Dailu, R., Sun, J., Shen, Z.K., Xu, X., 2012. Shallow creep on the Haiyuan fault (Gansu, China) revealed by SAR interferometry. Journal of Geophysical Research: Solid Earth 117. URL: `https://agupubs.onlinelibrary.wiley.com/doi/abs/10.1029/2011JB008732`, doi:`10.1029/2011JB008732`.

Lin, Y.n.N., Sladen, A., Ortega-Culaciati, F., Simons, M., Avouac, J.P., Fielding, E.J., Brooks, B.A., Bevis, M., Genrich, J., Rietbrock, A., Vigny, C., Smalley, R., Socquet, A., 2013. Coseismic and postseismic slip associated with the 2010 Maule Earthquake, Chile: Characterizing the Arauco Peninsula barrier effect. Journal of Geophysical Research: Solid Earth 118, 3142–3159. doi:`10.1002/jgrb.50207`.

Lindsey, E.O., Natsuaki, R., Xu, X., Shimada, M., Hashimoto, M., Melgar, D., Sandwell, D.T., 2015. Line-of-sight displacement from ALOS-2 interferometry: Mw 7.8 Gorkha earthquake and Mw 7.3 aftershock. Geophysical Research Letters 42, 6655–6661. doi:`10.1002/2015gl065385`.

Lohman, R.B., Simons, M., 2005. Some thoughts on the use of InSAR data to constrain models of surface deformation: Noise structure and data downsampling. Geochemistry, Geophysics, Geosystems 6. URL: `https://agupubs.onlinelibrary.wiley.com/doi/abs/10.1029/2004GC000841`, doi:`10.1029/2004GC000841`.

Ragon, T., Sladen, A., Simons, M., 2018. Accounting for uncertain fault geometry in earthquake source inversions I: theory and simplified application. Geophysical Journal International 214, 1174–1190. doi:`10.1093/gji/ggy187`.

Ragon, T., Sladen, A., Simons, M., 2019. Accounting for uncertain fault geometry in earthquake source inversions – II: Application to the Mw 6.2 Amatrice earthquake, Central Italy. Geophysical Journal International doi:`10.1093/gji/ggz180`.

Vigny, C., Socquet, A., Peyrat, S., Ruegg, J.C., Métois, M., Madariaga, R., Morvan, S., Lancieri, M., Lacassin, R., Campos, J., Carrizo, D., Bejar-Pizarro, M., Barrientos, S., Armijo, R., Aranda, C., Valderas-Bermejo, M.C., Ortega, I., Bondoux, F., Baize, S., Lyon-Caen, H., Pavez, A., Vilotte, J.P., Bevis, M., Brooks, B., Smalley, R., Parra, H., Baez, J.C., Blanco, M., Cimbaro, S., Kendrick, E., 2011. The 2010 Mw 8.8 Maule Megathrust Earthquake of Central Chile, Monitored by GPS. Science 332, 1417–1421. doi:`10.1126/science.1204132`.

Yadav, R.K., Roy, P.N.S., Gupta, S.K., Khan, P.K., Catherine, J.K., Prajapati, S.K., Kumar, A., Puviarasan, N., Bhu, H., Devachandra, M., Malik, J., Kundu, B., Debbarma, C., Gahalaut, V.K., 2017. Rupture model of Mw 7.8 2015 Gorkha, Nepal earthquake: Constraints from GPS measurements of coseismic offsets. Journal of Asian Earth Sciences 133, 56–61. URL: `http://www.sciencedirect.com/science/article/pii/S136791201630092X`.